Imaging quantum confinement with optical and POWER (perturbations observed with enhanced resolution) NMR

James G. Kempf[1], Michael A. Miller, and Daniel P. Weitekamp[2]

A. A. Noyes Laboratory of Chemical Physics, M/S 127-72, California Institute of Technology, Pasadena, CA 91125

Edited by Alexander Pines, University of California, Berkeley, CA, and approved November 11, 2008 (received for review July 7, 2008)

The nanoscale distributions of electron density and electric fields in GaAs semiconductor devices are displayed with NMR experiments. The spectra are sensitive to the changes to the nuclear-spin Hamiltonian that are induced by perturbations delivered in synchrony with a line-narrowing pulse sequence. This POWER (perturbations observed with enhanced resolution) method enhanced resolution up to 10^3-fold, revealing the distribution of perturbations over nuclear sites. Combining this method with optical NMR, we imaged quantum-confined electron density in an individual AlGaAs/GaAs heterojunction via hyperfine shifts. Fits to the coherent evolution and relaxation of nuclei within a hydrogenic state established one-to-one correspondence of radial position to frequency. Further experiments displayed the distribution of photoinduced electric field within the same states via a quadrupolar Stark effect. These unprecedented high-resolution distributions discriminate between competing models for the luminescence and support an excitonic state, perturbed by the interface, as the dominant source of the magnetically modulated luminescence.

GaAs | hyperfine or Knight shift | Stark effect | H-band photoluminescence

Imaging electron distributions and the electrostatic potentials that govern their transfer is a longstanding goal in diverse fields. Spin or charge transfer defines function in systems for photovoltaic and photosynthetic energy capture, ion channels, enzyme catalysis, spintronics, and molecular and nanoscale electronics. Success in imaging nanoscale electronic properties can lead to mechanistic understanding and provide guidelines to tune device performance or to modify natural systems for specialized applications. With its atomic-scale capabilities for nondestructive, noninvasive spectroscopy and imaging, NMR seems well suited to such characterization. However, NMR of solids is hampered by broad spectral lines because of static interactions that prevent measurement of small differences between sites that might otherwise reveal local electronic features with atomic detail.

Here, we present a general method whereby solid-state NMR surmounts this challenge and then apply it to image distributions of spin density and electric (E) field within an electronic state with dimensions ($\approx$10 nm) distributed over $\approx 10^5$ nuclei. The POWER (*p*erturbations *o*bserved *w*ith *e*nhanced *r*esolution) NMR approach, encodes small responses to a sample perturbation that is switched in synchrony with an NMR multiple-pulse line-narrowing sequence. The sequence removes the otherwise obscuring clutter of static spin interactions to yield a spectrum dominated by the desired perturbation with up to 3 orders-of-magnitude resolution enhancement. To further obtain the sensitivity and selectivity needed to isolate signals of local, nanoscale features from the bulk signal of a macroscopic sample, we combined the POWER approach with methods for optical NMR (ONMR). By using both optical nuclear polarization (ONP) (1–15) and optical detection (2–4, 6, 7, 9–13), ONMR provides the sensitivity needed for measurements on single epitaxial structures with selectivity for those sites that experience hyperfine coupling to photoexcited electrons in III–V semiconductors.

In the present light-induced POWER NMR, optical pulses were additionally used for a third purpose, to switch on perturbations specific to excited electronic states. These perturbations are synchronized with an rf sequence that toggles the orientations of nuclear spins to average away their static interactions, whereas the spin evolution in response to the switched perturbation accumulates to a measurable value. The optical excitation populates quantum-confined states that have distinct optical signatures by virtue of their proximity to an AlGaAs/GaAs interface. This introduces hyperfine interactions, which report on spin-polarized electron density, as the measured perturbation. By modifying the sample orientation and the timing of the optical pulses within the rf sequence, this approach was adapted to a second end, revealing the distribution of E field in the same electronic states via a linear quadrupolar Stark effect (LQSE).

The utility of ONMR in probing excited states has been long noted (3–5, 13) and used to explore electrostatics in quantum wells (16, 17), dots (10), and bulk materials (14, 15), but at a spectral resolution of no better than several kilohertz, set by many-body dipolar coupling between spins. Here, achieving resolution down to a few hertz, we demonstrate separate isolation of single-nucleus properties as the source of coherent spin evolution. The distribution of this property over nuclear sites images the electron wavefunction, without interference from dipolar couplings, and at spatial resolution approaching the atomic spacing. This is a unique experimental example of high-resolution POWER NMR. Our previous proposals suggested its use for atomic-layer resolution of spin density (18) or electric polarizability (19) in quantum wells, while a related proposal coupled with magnetic resonance force microscopy promises nanoscale materials imaging (20).

The Optical and POWER NMR Combination

The experimental timeline (Fig. 1) incorporates the time-sequenced ONMR approach (7), in which the phenomena of spin ordering by ONP, coherent spin evolution, and optical detection of the NMR signal are separately optimized in successive periods. The POWER evolution period t_1 entails multiple-pulse line narrowing, which, by itself, effectively suspends spin evolution as viewed stroboscopically at the end of the

Author contributions: J.G.K., M.A.M., and D.P.W. designed research; J.G.K. and M.A.M. performed research; J.G.K. and M.A.M. analyzed data; and J.G.K. and D.P.W. wrote the paper.

The authors declare no conflict of interest.

This article is a PNAS Direct Submission.

[1]Present address: Dept. of Chemistry and Chemical Biology, Rensselaer Polytechnic Institute, Troy, NY 12180.

[2]To whom correspondence should be addressed. E-mail: weitekamp@caltech.edu.

This article contains supporting information online at www.pnas.org/cgi/content/full/0806563106/DCSupplemental.

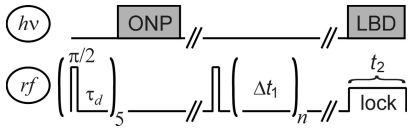

Fig. 1. General course of optical ($h\nu$) and radiofrequency (rf) excitation for time-sequenced ONMR. Optical nuclear polarization (ONP) is followed by NMR evolution for $t_1 = (n \times \Delta t_1)$ and spin-locked Larmor-beat optical detection (LBD) during t_2. RF irradiation of nonsignal nuclei is not shown. Breaks in the timeline can accommodate events such as adiabatic reorientation of the magnetic field (22). Saturation delays were $\tau_d \approx 1.5$ ms.

16-pulse cycle (21) of Fig. 2*A*. When optical excitation is synchronized with the rf pulses, spin evolution associated with the difference between ground- and excited-state interactions is introduced, and spin interactions that are common to these states and are first or second rank in the rf-modulated spin angular momentum are removed.

The alignment of NMR quantization axes with respect to the sample frame can be optimized separately for each task (ONP, t_1, and optical detection) by electronically reorienting the applied static magnetic field $\mathbf{B}_0$ (22). For ONP, $\mathbf{B}_0$ is along the [001] crystal axis. In that case, GaAs selection rules for circularly polarized (CP) excitation parallel (σ_+) or antiparallel (σ_-) to $\mathbf{B}_0$ yield highly polarized (25–100%), nonequilibrium electron spins (3). The transfer of that order to nuclear spins via fluctuations in the contact hyperfine interaction during 5 s of optical excitation yields ≈10% nuclear polarization in our system (9). This is a $\approx 10^3$-fold enhancement over the thermal value at 2 K. The nuclear magnetization then evolves through t_1, and optical detection follows in t_2. There the circularly polarized components, σ_+ and σ_-, of the photoluminescence (PL) are measured and combined to define its polarization, $\rho = (\sigma_+ - \sigma_-)/(\sigma_+ + \sigma_-)$. This quantity is modulated by magnetic fields (including hyperfine fields of nuclear origin) that are transverse to the optical axis through the Hanle effect (2). In particular, we use the Larmor-beat detection (LBD) method (9, 22), whereby ρ is

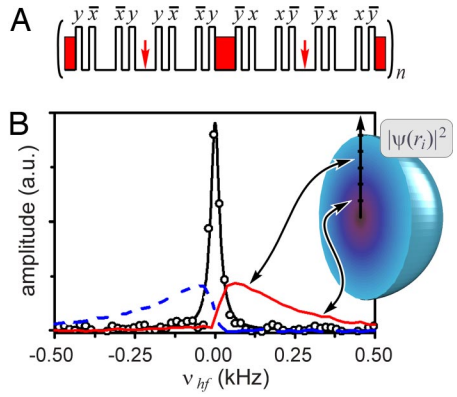

Fig. 2. ONMR/POWER NMR imaging of the electron distribution $|\Psi(r)|^2$. (*A*) Synchronization of σ_+ optical excitation (solid, red) with $\pi/2$ rf pulses of indicated phase. Arrows indicate alternative optical-pulse positions that yield the same imaging information, as described in the text. An essential modification of CLSW-16 (data not shown), in which select pulses are other than $\pi/2$ yields a homogenous frequency offset and improves resolution (*SI Methods*). (*B*) ^{71}Ga hyperfine distribution spectra and "light-off" reference spectrum collected without optical perturbation. Arrows indicate one-to-one correspondence of frequency and radial position for nuclei within a hydrogenic state with Bohr radius, $a_0^* \approx 10$ nm. The two spectral distributions resulted from the noted alternate placements of optical pulses (red, solid = as illustrated in *A*; blue, dashed = arrowed positions in *A*). The corresponding shift reversal also occurred with identical placement, but σ_- instead of σ_+ excitation, a photophysical effect of the inverted electron spin ($\langle S \rangle$ in Eq. **1**).

modulated by the transverse magnetization of signal (e.g., ^{71}Ga or ^{69}Ga) and reference (e.g., ^{75}As) nuclei. This variant of Hanle-effect optical detection has the advantages of providing an rf photocurrent linear in the precessing signal magnetization. The magnetization of the reference isotope is adjusted to optimize sensitivity by operating on the steep slope of the Hanle curve of ρ as a function of the total transverse field. Spin-locking of both signal and reference magnetizations prolongs the transients for seconds. The resulting advantages are selectivity to optically relevant sites and $\approx 10^5$-fold sensitivity gain (in addition to that from ONP) relative to traditional inductive detection of NMR.

Results and Discussion

AlGaAs/GaAs PL and Origins of the ONMR Signal. We studied a *p*-channel $Al_xGa_{(1-x)}As/GaAs$ ($x = 0.36$) single heterojunction grown by molecular beam epitaxy along [001]. [See supporting information (SI) Fig. S1.] Its PL spectrum (Fig. S2) exhibits bulk (interfacially distant) excitonic features in the range 818–819 nm, as well as the so-called *e* and *d* lines of the *H* band (23, 24) near 823 and 825 nm, respectively, which are induced by the presence of the interface. A band-to-acceptor carbon (BA_C) transition is observed near 832 nm. Through optical filtering and observations of PL polarization and Hanle-effect depolarization, we have shown that, in the present study, the *d* line is the carrier of the ONMR signal (see *SI Methods*). Its polarization of $\rho_{d\ \mathrm{line}} = 0.16$ with $B_0 = 246$ mT along [001] is extinguished with 5 mT applied along [110].

The nature of the electronic states that give rise to the *H*-band PL has been a matter of some debate (25–28). The earliest proposal suggested that the *e* and *d* lines result from recombination of free and donor-bound electrons with 2D interfacial holes (23, 25). Soon after, an excitonic model was proposed (26). More recent results support this and attribute the energy shift between *H*-band and bulk excitons to a spatially indirect character of *H*-band states caused by their localization in the tail of the interfacial E field (27, 28). The possibility remains that the two observed *H*-band features distinguish free and bound excitons perturbed by this field, whereas others continue to note evidence for nonexcitonic recombination at the interface (29). Our optical/POWER NMR combination is uniquely capable of quantifying differences among these several hypotheses, including intrastate distributions of spin density and E field, and the value of the interfacial E field at recombination sites.

Evidence for a Radial Exponential Spin-Density Distribution. The timing of the optical pulses in the POWER NMR sequences of Fig. 2*A* provides, as the dominant factor in NMR evolution,

$$\bar{\mathcal{H}}^{(0)}_{hf,i} = \left(-\frac{2}{3} b \Gamma \langle S \rangle \mu_0 g_0 \mu_B \gamma_n \left| \Psi(\mathbf{r}_i) \right|^2 \right) I_{z,i} = \nu_{hf,i}(\mathbf{r}_i)\ I_{z,i}, \qquad [1]$$

the contact-hyperfine Hamiltonian as averaged over the lifetime of the electron spin and over the period of the rf sequence via the duty factor b for optical excitation (Fig. 2*A*). Here, $I_{z,i}$ is the z component of spin angular momentum for the nucleus at $\mathbf{r}_i$, whose average hyperfine-induced precession frequency, $\nu_{hf}(\mathbf{r}_i)$, is proportional to b and to the time-averaged occupancy Γ and spin $\langle S \rangle$ of a photoexcited state with probability density $|\Psi(\mathbf{r}_i)|^2$. Remaining constants are the Bohr magneton, μ_B, nuclear gyromagnetic ratio, γ_n, and free-electron g factor, whose use, as opposed to the GaAs effective value, was justified by Paget (3). An alternative arrangement of optical pulses, noted by arrows in Fig. 2*A*, reverses the sign of the POWER hyperfine shift via the effect of the pulse sequence on $I_{z,i}$ in $\bar{\mathcal{H}}^{(0)}_{\mathrm{hf,i}}$.

The resulting ^{71}Ga POWER NMR spectra are shown in Fig. 2*B*, where hyperfine shifts ν_{hf} are relative to the center of a "light-off" reference obtained without optical pulses. Several observations confirm identification of the shifts in Fig. 2*B* with $\bar{\mathcal{H}}^{(0)}_{\mathrm{hf,i}}$. and, more specifically, with $\Psi(\mathbf{r}_i)$ of a quantum-confined state. First, the shift distribution changes sign for σ_- in place of σ_+ excitation, consistent with the paramagnetic nature of $\mathcal{H}_{hf}$, but inconsistent with an optically induced chemical shift. Second, the observed *distribution* of ν_{hf} is inconsistent with a freely diffusing electronic state, which would yield a motionally narrowed, nearly uniform shift. In addition, we can discount the possibility that the line shape reflects macroscopic inhomogeneity across the ≈350-μm profile of the optical beam on the sample, which would lead to variation in Γ. Such a distribution would vary in shape as the PL signal saturated with excitation power, whereas we found that the shape was retained over a range (1–20 W/cm^2) that passes from linear to saturated PL. We further rejected any notion of a macroscopic distribution of occupancy (Γ) by noting effects of spin diffusion that are only consistent with nanoscale origins of the hyperfine distribution, as quantified below. Finally, a hydrogenic wavefunction is expected for the *d* line of the *H* band because of its hypothesized origin as either an exciton or a donor-bound electron. These facts justify evaluation of the spin-density images by using Eq. **1** and the exponential radial probability density

$$|\Psi(r_i)|^2 = (d_i\Omega/\pi a_0^*)e^{-2r/a_0^*}, \qquad [2]$$

where electron density at the nuclear center (r_i) is specified by effective Bohr radius a_0^*, the volume Ω of a GaAs unit cell, and the element-dependent fractional distribution factor, d_i (3).

Analytical Model of the ONMR Signal. Eqs. **1** and **2** describe the radial dependence of the hyperfine shifts relative to the center of the localized state. To fit the POWER NMR line shape, it is also necessary to establish the radial variation of the signal amplitude per spin, which includes factors from both the ONP and optical detection periods. At least three processes bear on the problem and are active during both periods: optically induced hyperfine relaxation, spin diffusion of the resulting hyperpolarization, and other relaxation processes that tend to drive the polarization to negligibly small values. Relaxation and spin diffusion are not of concern during the relatively short evolution period t_1, but are included in the modeling by way of the decay rate of the light-off line shape.[†]

Spin diffusion presents the greatest challenge toward understanding the development of nuclear spin order during ONP and detection. To reveal the relative contributions of spin diffusion, hyperfine fluctuations, and other processes, the same POWER NMR data, can be used to display hyperfine images at *each* value of t_2. As shown in Fig. 3, this reveals decay of the LBD NMR signal in t_2 as a function of ν_{hf}. We fit transients at fixed ν_{hf} to single exponentials with time constants $T_{1\rho}(\nu_{hf})$ for spin-locked relaxation. The Fig. 3 *Inset* plots $(T_{1\rho})^{-1}$ vs. $(\nu_{hf})^2$ for ^{71}Ga, along with two limiting expectations: negligible (solid line) and fast (dashed line) spin diffusion. The former case incorporates only a hyperfine relaxation rate $(T^{hf}_{1\rho})^{-1}$ proportional to $|\mathcal{H}_{hf}|^2$ and a "background" contribution $(T^{B}_{1\rho})^{-1}$ that we took as spatially uniform. In contrast, fast spin diffusion would render relaxation independent of ν_{hf} by averaging any spatial variation in the overall time constant.

Our data indicate an intermediate case, in which the influence of spin diffusion increases with ν_{hf}, i.e., it is most prominent in the small *r* region of the spectral distribution. The diminishing effects at sites with greater *r* result from corresponding small, slowly varying hyperfine shifts. Thus, a linear fit to this regime ($\nu_{hf} \lesssim 200$ Hz) reveals $T^B_{1\rho}(^{71}\mathrm{Ga}) = 4.8 \pm 0.4$ s, and, from a separate experiment, $T^B_{1\rho}(^{69}\mathrm{Ga}) = 2.9 \pm 0.1$ s. Further justification of these values as diffusion free, and analysis of the physical origins of $T^B_{1\rho}$ are provided in *SI Discussion*. The decomposition into hyperfine and other terms allows quantitative modeling of the hyperfine distribution.

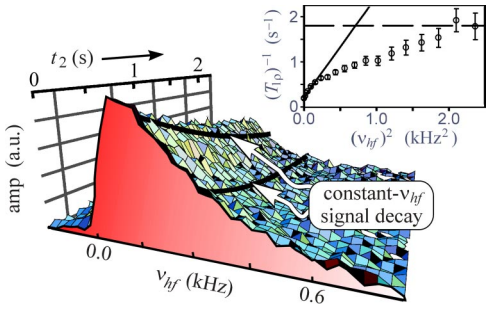

Fig. 3. Hyperfine distribution for ^{71}Ga as a function of the optical detection time t_2. *Inset* shows relaxation constants from exponential fits to each constant-ν_{hf} decay. Uncertainties are 95% confidence intervals. Solid and dashed lines are the hypothetical cases of negligible and fast spin diffusion.

Importantly, these observations confirm the nanoscale origin of the distribution of hyperfine shifts. Diffusion effects are clear within 2.0 s of optical detection, consistent with a distance scale of 10 nm ($\approx\sqrt{4Dt/\pi}$) assuming a diffusion constant $D(^{71}\mathrm{Ga})$ ≈4 × 10^{-13} cm^2/s (4, 30). To proceed from here with explicit modeling of spin diffusion would be, at best, an uncertain prospect. A theoretical framework is lacking for diffusion among spins-3/2 (all GaAs isotopes), although previous attempts to apply spin-1/2 models (5, 14, 15, 31) yielded results discordant with expectations on the nature of electronic states involved in ONP. A more reliable approach for now is to eliminate the need for detailed modeling of spin diffusion by turning to sufficiently short ONP and optical detection periods. In this limit, the signal of the *i*th nucleus is

$$S(r_i, t_{\mathrm{ONP}}, t_1, t_2) = A(r_i, t_{\mathrm{ONP}}, t_2)(e^{-\pi\Delta\nu_i t_1}\cos(\omega_i(r_i)t_1)), \qquad [3]$$

where $\omega(r_i)$ and $(\pi\,\Delta\nu_i)$ are the frequency and Lorentzian decay for t_1, and $A(r_i, t_{\mathrm{ONP}}, t_1)$ is composed of 3 factors: an arbitrary scale A_0, the polarization from ONP

$$P(t_{\mathrm{ONP}}, r_i) = \frac{\rho_0 T_1^Q + \rho_T T_1^{hf}(r_i)}{T_1^Q + T_1^{hf}(r_i)}\left(1 - e^{\frac{-t_{\mathrm{ONP}}(T_1^Q + T_1^{hf}(r_i))}{T_1^Q T_1^{hf}(r_i)}}\right), \qquad [4]$$

with initial condition $P(0, r_i) = 0$, and the signal function for detection,

$$S_2(t_2, r_i) = (|\Psi(r_i)|^2/|\Psi(0)|^2)\, e^{\frac{-t_2(T^B_{1\rho} + T_1^{hf}(r_i))}{T^B_{1\rho} T_1^{hf}(r_i)}}, \qquad [5]$$

where the position-dependent prefactor accounts for the linear dependence of the LBD signal on $\mathcal{H}_{hf}$. The steady-state limits of optically induced (ρ_0) and thermal (ρ_T) relaxation acting separately are approached with time constants $T_1^{hf}(r_i)$ and T_1^Q stemming from hyperfine and quadrupolar fluctuations, respectively. The proportionality of $T_1^{hf}(r_i)$ to $|\mathcal{H}_{hf}|^{-2}$ with Eqs. **1** and **2** gives

$$T_1^{hf}(r_i) = T_1^{hf}(0)e^{+4r_i/a_0^*}. \qquad [6]$$

Finally, Eqs. **4** and **5** assume uniform T_1^Q and $T^B_{1\rho}$, and replace the hyperfine contribution to spin-locked relaxation with $T_1^{hf}(r_i) \simeq T^{hf}_{1\rho}(r_i)$, which is justified since the rate of electron spin relaxation

[†]Although not pertinent to present experiments, cases where the light-off lineshape does not accurately represent the point-spread function of the POWER NMR spectrum are discussed in *SI Methods*.

is far faster than the nuclear Larmor and Rabi frequencies relevant to each time constant.

Quantifying the Nanoscale Distribution of Electron Spin Density. To apply this analytical model, we determined $T_0^{hf}(r_i)$ and T_1^Q by recording the ONMR signal at $t_1 = 0$ as a function of t_{ONP} (0–30 s) and t_2 (0–2.25 s). The 2-dimensional data were fit to Eq. **3** with the addition of DC offset (A_1) and omission of negligible terms (*SI Methods*). Four-parameter [$A_0, A_1, T_0^{hf}(r_i)$, and T_1^Q] nonlinear least-squares fits were made to both ^{71}Ga and ^{69}Ga datasets. To obtain results unperturbed by spin diffusion, we used a fitting scheme with iterative descent to short-timescale data (*SI Methods*), which revealed convergence of $(T_1^{hf}(0))^{-1}$ on a plateau at short ($t_{ONP}^{max} < 2.0$ s, $t_2^{max} < 1.0$ s) timescales, and established $(T_1^Q)^{-1}$ as negligible. Parameter variation over the range of t_2^{max} was much less pronounced than with t_{ONP}^{max}, as expected due to attenuation of spin diffusion by the LBD spin-lock field. Averaging points in the noted plateau gave $T_1^{hf}(0) \approx 16$ and 90 ms (with 9 and 12% standard deviation) for ^{71}Ga and ^{69}Ga, respectively, which are close to values (72 ± 45 and 120 ± 72 ms) estimated by Paget for a similar electronic system (4, 30).

The hyperfine distribution may now be interpreted as a spin-density image by resorting to short ONP times to obviate spin diffusion, with corresponding use of Eqs. **1–6** with measured $T_1^{hf}(0)$ and $T_{1\rho}^B$, and as simplified as above by $\rho_T \simeq 0$ and $(T_{1\rho}^Q)^{-1} \simeq 0$ (*SI Methods*). The ^{71}Ga spectra at t_{ONP} = 144, 240, 720 ms and 3.0 s (Fig. 4*A*) were compared with simulations in which the signal function was integrated over the experimental range of t_2, and summed over contributions from individual lattice sites in a sphere to r_{max} = 70 nm. We assumed a uniform line width of $\Delta\nu_i$ = 32 Hz taken from the light-off experiment, Γ = 1 during light-on periods (justified by saturation of ν_{hf} at the 10 W/cm^2 optical power used), and a_0^* = 10.37 nm, which is consistent with electron-spin distributions of either an exciton or a donor-bound electron. (For additional parameter details, see Table S1.)

A grid search over A_0 and $\langle S\rangle$ located the reduced-χ^2 optimum for t_{ONP} = 144 ms, the image least perturbed by spin diffusion. The fitted values are similar when using t_{ONP} = 240 or 720 ms data, but not for t_{ONP} = 3.0 s data (Table S2). By using the parameters from the 144-ms fit, excellent agreement resulted for t_{ONP} = 144, 240, 720 ms (χ^2 = 1.0, 1.3, 1.8), but not for 3.0 s (χ^2 = 12.5). Fig. 4*A* shows the observed spectra with this set of simulations. An indication of consistency is that the t_{ONP} = 144-ms fit gave $\langle S\rangle = 0.15_3$, which is indistinguishable from the values measured from the PL polarization of the *H* band *e* and *d* lines [$\rho = \langle S\rangle$ from the selection rules in the present case (3, 30)]. At t_{ONP} = 3.0 s, the large discrepancy between experiment and simulation with Eq. **3** (solid line in Fig. 3 *Inset*) is understood as the effects of spin diffusion, which yields a net transfer of spin order, and hence signal amplitude, to large r where ν_{hf} is small.

The image of electron spin density is established by the best fit at t_{ONP} = 144 ms, which specifies the one-to-one relation of frequency (ν_{hf}) to radial position (r/a_0^*). With this, we could label the upper horizontal axis for (r/a_0^*) in Fig. 4*A*. Radial resolution, $\Delta r = \Delta\nu\,(dr(\nu_{hf})/d\nu_{hf})$, varies linearly with $\Delta\nu$ and exponentially with (r/a_0^*) [see *SI Methods*] and is plotted in Fig. 4*B* aligned to the images in Fig. 4*A*. With the observed $\Delta\nu$ = 32 Hz, the atomic-resolution threshold [$(a/2^{1/2}) \approx 0.4$ nm, where a is the GaAs lattice constant] is crossed near (r/a_0^*) = 1, as indicated in Fig. 4*B*, whereas the range (r/a_0^*) = 0.5–2.0 corresponds to Δr from 0.2 to 3.6 nm. If instead, one assumes the best spectral resolution ($\Delta\nu$ = 4 Hz) we have obtained with this technique and sample (22), the entire image would exceed atomic-resolution (dashed curve in Fig. 4*B*). Because the imaged quantity varies radially and the separation of discrete radii for the lattice sites is less than the lattice constant, no atomically resolved peaks are apparent even where the atomic-resolution threshold has been surpassed. However, in a system where the imaged quantity varies along a lattice vector, such as a quantum well, individual peaks from single atomic layers are predicted at similar spectral resolution (18, 19).

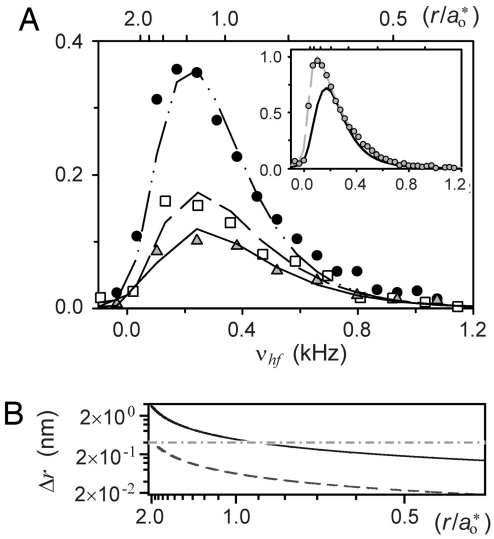

Fig. 4. Images of the electronic distribution, $|\Psi(r)|^2$. (*A*) ^{71}Ga hyperfine distributions from t_{ONP} = 144 (triangles), 240 (squares) and 720 (circles) ms, and 3.0 s (*Inset*). Lines are simulations described in the text. The two at t_{ONP} = 3.0 s used analytical (solid) or empirical (dashed) radial weighting of signal amplitudes contributed by single nuclei. Interpretation of spectra as images of the electron density enabled labeling the uppermost axis as distance (r/a_0^*) from the hydrogenic center. The distribution at t_{ONP} = 144 results from sites within (r/a_0^*) < 1.5, or ≈10^5 nuclei per state. (*B*) Radial resolution (Δr) vs. position, with atomic-resolution cutoff at the horizontal (dash-dot) line. The upper curve assumes spectral resolution ($\Delta\nu$ = 32.0 Hz) from *A*, whereas the lower incorporates the best obtained to date ($\Delta\nu$ = 4.1 Hz) to indicate resolving potential.

Finally, 2 significant advances beyond wavefunction imaging must be noted. First, images here that are perturbed by spin diffusion ($t_{ONP} > 1$ s) provide an unprecedented, well-defined testing ground for theories of diffusion among spins > ½, and of diffusion frustrated by inhomogeneous spin interactions (31). These nanoscale, short-timescale results complement those from previous schemes that probe diffusion at micron scales (32) or over long timescales that result in mixed nano/micron scale information (14). The second advance is that fitted hyperfine distributions enable *replacement* of the diffusion-free analytical signal weights (Eqs. **3–6**) with an empirical function, $A_E(r, t_{ONP}, t_2^{max})$. Development of such is valid *at any ONP time*, even when diffusion is significant. (For details, see Fig. S3 and *SI Methods*.) We demonstrated empirical weighting in the Fig. 4*A* *Inset* (t_{ONP} = 3.0 s), resulting in a shape (dashed line) with χ^2 = 1. Remarkably, the now obviated limitation to short ONP times allows POWER imaging over a spatial distribution and with signal-to-noise that may be optimized by unrestricted choice of t_{ONP}. Furthermore, empirical weights enable spectral simulations *without adjustable parameters* whether or not spin diffusion contributes and for observables beyond the hyperfine interaction, where position vs. frequency may not be one-to-one (as for the LQSE).

The Nanoscale Distribution of Electric Field. We obtained a distinct POWER NMR spectrum to assess the E field distribution of the photoexcited state. In contrast to spin-density imaging, this experiment is additionally sensitive to the fate of the photoexcited hole. We were thus able to distinguish between models (exciton vs. donor-bound electron) for the origin of *d*-line PL. As in the hyperfine case, the experiment reveals the local response to populating the *d*-line state by optical excitation. However, by

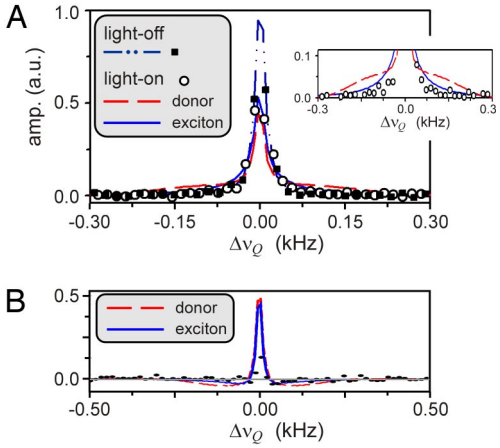

Fig. 5. ONMR/POWER NMR imaging of the E field distribution from the carrier state. (*A*) Light-on and off ^{71}Ga spectra (points) with simulations (lines) for the indicated models. Quadrupole splitting $\Delta\nu_Q$ is referenced to the light-off position. (*Inset*) Expansion of regions with quadrupole satellite amplitude. (*B*) Light-off minus on difference for spectra (points) and simulations in *A*.

placing optical pulses at *both* illustrated and arrowed positions in Fig. 2*A*, we select only optically induced spin interactions that are bilinear in I_z, such as the LQSE. The mechanism of the LQSE is that slight E-field-induced distortions of both the lattice and local electron density induce electric-field gradients and, hence, nuclear quadrupole interactions that are *linear in the E field* at a particular nuclear site (19, 33, 34). The result is a nuclear quadrupole splitting ($\Delta\nu_Q$), the symmetric separation between peaks in a 3:4:3 triplet of the otherwise degenerate central ($+\frac{1}{2} \leftrightarrow -\frac{1}{2}$) and satellite ($\pm\frac{3}{2} \leftrightarrow \pm\frac{3}{2}$) transitions of a spin $\frac{3}{2}$. This effect also requires distinct magnetic-field direction during t_1. With $\mathbf{B}_0$ along the [110] axis of GaAs, the LQSE yields $\Delta\nu_Q$ linear in the component (E_{001}) of the E field along [001] (19, 33, 34), whereas the related Hamiltonian ($\mathcal{H}_{LQSE}$) vanishes in the orientation used for hyperfine imaging ($\mathbf{B}_0$//[001]) (19, 33). Finally, the selective placement of optical pulses ensures POWER-NMR conversion of $\mathcal{H}_{LQSE}$ to an observable average $\overline{\mathcal{H}}^{(0)}_{LQSE}$ (19).

Spectra of the photoexcited LQSE and a light-off reference are shown in Fig. 5*A*. The most obvious change is the amplitude reduction at the central transition ($\Delta\nu_Q = 0$) of the light-on, LQSE spectrum. This is consistent with redistribution of intensity into broad, field-induced quadrupolar satellites corresponding to broad distributions of E_{001}, as expected from calculated profiles of candidate *d*-line states (Fig. S4). To emphasize the significance of the observed change, Fig. 5*B* shows the light-off minus light-on difference between spectra in Fig. 5*A*, yielding a maximum change of 17 times the rms noise amplitude. Similar difference spectra were reproduced in 4 separate on/off experiment pairs. As a control, repetition in the LQSE-insensitive orientation ($\mathbf{B}_0$//[001] during t_1) yielded no on/off difference.

To evaluate candidate electronic states, we compared the active-LQSE result ($\mathbf{B}_0$//[110]) to simulations assuming either a donor-bound electron or an exciton with fixed center of mass. As shown in Fig. 5 *Inset*, the donor-bound electron model yields a buildup of satellite amplitude near the baseline that is not consistent with the observed spectrum ($\chi^2 = 9.1$). In contrast the fixed-exciton model provides a good match ($\chi^2 = 3.1$). *No adjustable parameters* were used in these simulations, which included empirical radial weights (from a hyperfine image at matching $t_{ONP} = 5$ s) and the same summation over lattice sites described for hyperfine simulations. In each model, the electron distribution is given by Eq. **2** with $a_0^* = 10.37$ nm, consistent with our spin-density images. However, the fixed-exciton model includes co-confinement of a photoexcited hole (1.56-nm Bohr radius), which greatly changes the radial profile of E_{001} (Fig. S4) to yield consistency with the observed spectrum (Fig. 5).

More complex many-body states, such as an exciton bound to a neutral donor, may yield similar or improved agreement. These likewise exhibit radial distributions of electron spin density and photo-carrier E field, and are more easily reconciled with current knowledge of the *H*-band electronic states (27, 28). Finally, improved simulations might also result by allowing displacement of electron and hole centers of mass by the interfacial E field (E_{int}). We measured $E_{int}^{001} \leq (1.26 \pm 0.07)$ kV/cm via LQSE-induced differences in ^{71}Ga spin-echo line shapes for $\mathbf{B}_0$ along [001] and [110] (Fig. S5). This value matches the exciton-dissociation limit (30), and is thus consistent with our description of the *d*-line state. It also corresponds to >1-μm distance from the interface, thus excluding the possibility that the interface luminescence is the result of electron recombination with 2D interfacial holes (Fig. S6).

To conclude this evaluation, we have shown our results correspond to the *d*-line state due to optical filtering of the ONMR signal and the remarkable correspondence of $\langle S \rangle$ derived from PL polarization and from our hyperfine imaging spectra. That this state is localized is demonstrated by observation of a radial hydrogenic distribution of hyperfine shifts, whereas its nanoscale dimensions are proven by the spatially dependent spin-relaxation study. The observed LQSE distribution excludes the donor-bound electron model, whereas involvement of 2D localized carriers is eliminated by the measured interface field. All results support a bound excitonic species as the *d*-line state. It yields an exceptional ($\chi^2 = 1$) fit to the image of spin-polarized electron density that agrees with $\langle S \rangle$ from polarized PL. The model is also consistent with observations of both intrastate and interfacial electrostatic effects at the sites of localization. This single-state model is the simplest that survives our suite of experiments, whereas any other would require multistate descriptors that are not justified by our results.

Summarizing spectroscopic and imaging advances, we used POWER NMR, the cyclic perturbation of the sample in synchrony with rf excitation, as a high-resolution probe to image distributions of spin density and E field at nanoscale dimensions. Three orders-of-magnitude enhanced spectral resolution translated to spatial resolution down to the atomic spacing in hyperfine images of photoexcited electron spin density. Nanoscale hyperfine distributions have been revealed as NMR line shapes with unprecedented resolution. Similarly unprecedented is our high-resolution measurement of E fields via NMR Stark effects, which further traced the fate of the photoexcited hole. To interpret spectra as images, analytical expressions incorporating measured parameters were developed. Fits to radially resolved signal decay demonstrate nanoscale variation in nuclear spin-relaxation rates, uncovering the effects of spin diffusion, but validating analytical, diffusion-free fits to hyperfine distributions at $t_{ONP} \leq 720$ ms. Images at longer t_{ONP} provide an opportunity to develop theoretical models of spin-$\frac{3}{2}$ diffusion. Here, they were used, along with the one-to-one relation between position and frequency established at $t_{ONP} = 144$ ms, to define an empirical function to weight the signal vs. radial position. Its use is valid regardless of contributions from spin diffusion and also enabled us to interpret POWER NMR spectra of the radial E field via the LQSE and establish the excitonic nature of the electronic state.

The POWER NMR methods used to these ends are extensible to a wide variety of systems, from biomolecules to semiconductor devices, in which controlled transport of charge or spin is essential to function. A subset of such applications will be amenable to imaging effects of photophysical perturbations, although a more general route is possible by applying external E fields as the perturbation source (19). Furthermore, although we

used ONMR enhancements to gain sensitivity and selectivity for signals from subpopulations of perturbed sites, these are unnecessary in samples with regular structure (crystals) or those consisting of a molecular ensemble (powders). Material samples that do require selectivity may be amenable to other specialized means of enhancement (35–38) or bulk-signal deconvolution. POWER NMR may be particularly valuable as a biomolecular Stark probe. Using a convenient molecular probe, Boxer has directly measured *vibrational* Stark effects in an enzyme active site (39), where local electrostatics can dramatically alter function. POWER NMR may provide more general and noninvasive Stark probes, such as native carbonyl or amide groups. Biomolecular NMR Stark effects have been inferred from variations in chemical shifts and quadrupole splittings with *intramolecular* E fields (40), but are poorly understood and too small to measure at practical *applied* E fields. This limitation, due to the broad lines in traditional NMR, is lifted by the POWER approach.

Methods

Critical experiment details include sample temperature ($T \approx 2$ K), optical excitation (802.1 nm) and detection (832 $\pm$ 5 nm bandpass) wavelengths, and $B_0 = 246$ or 57.6 mT along [001] or [110] crystal axes, respectively. In both *SI Methods* and ref. 22, we detail the sample, apparatus, and NMR parameters, as well as protocols for LBD optical and POWER NMR.

ACKNOWLEDGMENTS. We thank Frank Grunthaner of the National Aeronautics and Space Administration Jet Propulsion Laboratory for providing the sample, Doran Smith of the U.S. Army Research Laboratory for the Schrödinger–Poisson solver used to calculate the interfacial E field, and Lou Madsen of Virginia Tech for critical reading of the manuscript. This work was supported by National Science Foundation Grant CHE-9612226.

1. Lampel G (1968) Nuclear dynamic polarization by optical electronic saturation and optical pumping in semiconductors. *Phys Rev Lett* 20:491–493.
2. Ekimov AI, Safarov VI (1972) Optical electron-nuclear resonance in semiconductors. *JETP Lett* 15:319.
3. Paget D, Lampel G, Sapoval B, Safarov VI (1977) Low field electron-nuclear spin coupling in gallium arsenide under optical pumping conditions. *Phys Rev B* 15:5780–5796.
4. Paget D (1982) Optical-detection of NMR in high-purity GaAs: Direct study of the relaxation of nuclei close to shallow donors. *Phys Rev B* 25:4444–4451.
5. Bowers CR (1998) Microscopic interpretation of optically pumped NMR signals in GaAs. *Solid State NMR* 11:11–20.
6. Flinn GP, Harley RT, Snelling MJ, Tropper AC, Kerr TM (1990) Optically detected nuclear magnetic resonance of nuclei in a quantum well. *Semicond Sci Technol* 5:533–537.
7. Buratto SK, Shykind DN, Weitekamp DP (1991) Time-sequenced optical nuclear magnetic resonance of gallium arsenide. *Phys Rev B* 44:9035–9038.
8. Barrett SE, Tycko R, Pfeiffer LN, West KW (1994) Directly detected nuclear magnetic resonance of optically pumped GaAs quantum wells. *Phys Rev Lett* 72:1368–1371.
9. Marohn JA, *et al.* (1995) Optical Larmor beat detection of high-resolution nuclear magnetic resonance in a semiconductor heterostructure. *Phys Rev Lett* 75:1364–1367.
10. Gammon D, *et al.* (1997) Nuclear spectroscopy in single quantum dots: Nanoscopic raman scattering and nuclear magnetic resonance. *Science* 277:85–88.
11. Kikkawa JM, Awschalom DD (2000) All-optical nuclear magnetic resonance in semiconductors. *Science* 287:473–476.
12. Eickhoff M, Suter D (2004) Pulsed optically detected NMR of single GaAs/AlGaAs quantum wells. *J Magn Reson* 166:69–75.
13. Suter D, Klieber R (2007) Spins as probes of different electronic states. *Concepts Magn Reson Part A* 30A:116–126.
14. Paravastu AK, Reimer JA (2005) Nuclear spin temperature and magnetization transport in laser-enhanced NMR of bulk GaAs. *Phys Rev B* 71:045215.
15. Ramaswamy K, Mu, S Hayes SE (2006) Light-induced hyperfine Ga-69 shifts in semiinsulating GaAs observed by optically polarized NMR. *Phys Rev B* 74:153201.
16. Tycko R, Barrett SE, Dabbagh G, Pfeiffer LN, West KW (1995) Electronic states in gallium arsenide quantum wells probed by optically pumped NMR. *Science* 268:1460–1463.
17. Eickhoff M, Fustmann S, Suter, D (2005) Light-induced Knight shifts in GaAs/AlxGa1-xAs quantum wells. *Phys Rev B* 71:195332.
18. Buratto SK, Shykind DN, Weitekamp DP (1992) Can nuclear magnetic resonance resolve epitaxial layers? *J Vac Sci Technol B* 10:1740–1743.
19. Kempf JG, Weitekamp DP (2000) Method for atomic-layer-resolved measurement of electric polarization fields by nuclear magnetic resonance. *J Vac Sci Technol B* 18:2255–2262.
20. Kempf JG, Marohn JA (2003) Nanoscale Fourier-transform imaging with magnetic resonance force microscopy. *Phys Rev Lett* 90:087601.
21. Cho HM, Lee CJ, Shykind DN, Weitekamp DP (1985) Nutation sequences for magnetic resonance imaging in solids. *Phys Rev Lett* 55:1923–1926.
22. Kempf JG, *et al.* (2008) An optical NMR spectrometer for Larmor-beat detection and high-resolution POWER NMR. *Rev Sci Instrum* 79:063904.
23. Yuan YR, Pudensi MAA, Vawter GA, Merz JL (1985) New photoluminescence effects of carrier confinement at an AlGaAs/GaAs heterojunction interface. *J Appl Phys* 58:397–403.
24. Krapf M, Denninger G, Pascher H, Weimann G, Schlapp W (1990) Optically detected conduction electron-spin-resonance, Overhauser shift and nuclear-magnetic-resonance in *p*-GaAlAs/GaAs heterostructures. *Superlattices Microstruct* 8:91–96.
25. Ossau W, Bangert E, Weimann G (1987) Radiative recombination of a 3D-electron with a 2D-hole in *p*-type GaAs/(AlGa)As heterojunctions. *Solid State Commun* 64:711–715.
26. Yuan YR, Merz JL, Vawter GA (1988) The characteristics of photoluminescence at a GaAs/AlGaAs Interface. *J Lumin* 40-1:755–756.
27. Shen JX, *et al.* (1999) Photoluminescence in modulation-doped GaAs/Ga(1-x)Al (x)As heterojunctions. *Phys Rev B* 59:8093–8104.
28. Shen JX, Pittini R, Oka Y, Kurtz E (2000) Exciton dynamics in GaAs/Ga(1-x)Al(x)As heterojunctions and GaAs epilayers. *Phys Rev B* 61:2765–2772.
29. Bryja L, *et al.* (2002) Impurity-related emission in the photoluminescence from p-type modulation doped $Al_{(1-x)}Ga_xAs$/GaAs heterostructures. *Solid State Commun* 122:379–384.
30. Kempf JG (2000) Probing quantum confinement at the atomic scale with optically detected NMR. PhD thesis (California Institute of Technology, Pasadena, CA).
31. Deng CX, Hu XD (2005) Nuclear spin diffusion in quantum dots: Effects of inhomogeneous hyperfine interaction. *Phys Rev B* 72:165333.
32. Zhang WR, Cory DG (1998) First direct measurement of the spin diffusion rate in a homogenous solid. *Phys Rev Lett* 80:1324–1327.
33. Gill D, Bloembergen N (1963) Linear stark splitting of nuclear spin levels in GaAs. *Phys Rev* 129:2398–2402.
34. Dumas KA, Soest JF, Sher A, Swiggard EM (1979) Electrically induced shifts of the GaAs nuclear spin levels. *Phys Rev B* 20:4406–4415.
35. Bowers CR, Weitekamp DP (1987) Para-hydrogen and synthesis allow dramatically enhanced nuclear alignment. *J Am Chem Soc* 109:5541–5542.
36. Rugar D, *et al.* (1994) Force detection of nuclear-magnetic-resonance. *Science* 264:1560–1563.
37. Madsen LA, Leskowitz GM, Weitekamp DP (2004) Observation of force-detected nuclear magnetic resonance in a homogeneous field. *Proc Natl Acad Sci USA* 101:12804–12808.
38. Wickramasinghe NP, Shaibat M, Ishii Y (2005) Enhanced sensitivity and resolution in H-1 solid-state NMR spectroscopy of paramagnetic complexes under very fast magic angle spinning. *J Am Chem Soc* 127:5796–5797.
39. Suydam IT, Snow CD, Pande VS, Boxer SG (2006) Electric fields at the active site of an enzyme: Direct comparison of experiment with theory. *Science* 313:200–204.
40. Augspurger JD, Dykstra CE, Oldfield E (1991) Correlation of carbon-13 and oxygen-17 chemical shifts and the vibrational frequency of electrically perturbed carbon monoxide: A possible model for distal ligand effects in carbonmonoxyheme proteins. *J Am Chem Soc* 113:2447–2451.